Morphology and dynamic scaling analysis of cell colonies with linear growth fronts

M. A. C. Huergo, M. A. Pasquale, A. E. Bolzán, and A. J. Arvia
Instituto de Investigaciones Fisicoquímicas Teóricas y Aplicadas (INIFTA), UNLP, CONICET, Sucursal 4, Casilla de Correo 16, 1900 La Plata, Argentina

P. H. González
Cátedra de Patología B, Facultad de Ciencias Médicas, Universidad Nacional de La Plata, Calle 60 y 120, 1900 La Plata, Argentina
(Received 23 May 2010; revised manuscript received 28 July 2010; published 14 September 2010)

The growth of linear cell colony fronts is investigated from the morphology of cell monolayer colonies, the cell size and shape distribution, the front displacement velocity, and the dynamic scaling analysis of front roughness fluctuations. At the early growth stages, colony patterns consist of rather ordered compact domains of small cells, whereas at advanced stages, an uneven distribution of cells sets in, and some large cells and cells exhibiting large filopodia are produced. Colony front profiles exhibit overhangs and behave as fractals with the dimension $D_F=1.25\pm0.05$. The colony fronts shift at 0.22 ± 0.02 μm min^{-1} average constant linear velocity and their roughness (w) increases with time (t). Dynamic scaling analysis of experimental and overhang-corrected growth profile data shows that w versus system width l log-log plots collapse to a single curve when l exceeds a certain threshold value l_o, a width corresponding to the average diameter of few cells. Then, the influence of overhangs on the roughness dynamics becomes negligible, and a growth exponent $\beta=0.33\pm0.02$ is derived. From the structure factor analysis of overhang-corrected profiles, a global roughness exponent $\alpha_s=0.50\pm0.05$ is obtained. For $l>200$ μm, this set of exponents fulfills the Family-Vicsek relationship. It is consistent with the predictions of the continuous Kardar-Parisi-Zhang model.

DOI: 10.1103/PhysRevE.82.031903 PACS number(s): 87.16.dj, 87.17.Ee, 87.18.Hf, 89.75.Da

I. INTRODUCTION

Statistical mechanics offers robust tools for deriving theoretical and experimental information related to the growth dynamics of condensed materials [1,2]. One of these tools, used for studying the evolution of rough interfaces, is the dynamic scaling analysis based on concepts from the theory of stochastic processes [3–5]. This approach permits the evaluation of the so-called scaling exponents that in simpler growth models are α, the roughness exponent characterizing the saturated interface roughness; β, the growth exponent related to the roughness kinetics; and $z=\alpha/\beta$, the dynamic exponent. From a set of these exponents the likely universality class, to which a certain growth process belongs, can be inferred [2,6].

In the last decades the dynamic scaling theory has been applied to investigate the growth mechanism of a variety of heterogeneous systems including biological ones such as cell lines and tumors [7,8] and bacterial [9–12] colonies. Pioneering work in the field of bacterial colony growth [10–13] has been oriented to investigating the cooperative bacterial motion in relation to the complex structure of colonies and the feasibility of the scaling analysis of colony front profiles. From the scaling analysis of *Escherichia coli* and *Bacillus subtilis* linear colonies, produced by sticking a sterile string inoculated with bacteria on agar plates, a value of $\alpha=0.78$ has been reported [13]. This figure has been interpreted as an indication of the presence of correlation effects in the formation of the colony interface. Most of the studies including those on three-dimensional (3D) tumor growth have been aimed to learn basic dynamic aspects that would be of interest to develop possible therapies [14]. In this context, it appears that a combination of physical and biological strategies would result in a promising step forward in dealing with the global study of the dynamics of cell colonies, particularly those related to specific diseases [7,15–17].

Dynamic scaling analysis was applied to the study of both colonies of different cell lines and tumors, and from the resulting scaling exponents, their growth dynamics was associated with the molecular beam epitaxy universality class [7,8]. This growth dynamics involves the formation of new cells at the colony growth front and diffusion of newborn cells toward concavities. However, the scaling analysis was performed on cell colonies and tumors that grew radially, as occurs spontaneously in nature, using models that were developed for a linearly growing system [2]. This drawback was later pointed out [18–20] and new attempts to model the growth of cell colonies have been proposed [20–22]. In fact, the complex nature of cell colonies entails difficulties for developing adequate theoretical models that keep pace with the experimental data of growth dynamics. Such complications arise when the growth of colonies is accompanied, for instance, by changes in their configuration, a situation that has only recently received particular attention [21,22].

In this paper we consider the possibility of obtaining data that can be directly processed with the mathematical formalism of the dynamic scaling analysis that has been derived from theoretical linear growth models [2]. For this purpose, we developed experimental strategies for growing linear cell colony fronts in Petri dishes. This approach allows performing a reliable scaling dynamic analysis of colony expansion dynamics and permits distinguishing some unique contributions to the colony growth kinetics.

The experimental strategies are applied to *in vitro* growth of *Vero* (African Green Monkey kidney) cell colonies. These cells, unlike primary cells, continue growing and dividing as long as adequate culture conditions are maintained. They exhibit an almost null contact inhibition and, although they are

not tumorigenic, at least in a passage lower than 191 [23,24], they show an invasive behavior like that of cancer cells. Phenomenological and dynamic scaling analysis of linear growth fronts results in data to bring out the likely colony growth dynamics and to envisage possible complications induced by changes in the colony morphology, its degree of disorder, and the appearance of local cooperative fluctuations in cell concentration and pressure gradients. The latter can generate driving forces that assist the local biomechanically mediated transport of cells from the bulk of the colony to the interface.

II. EXPERIMENT

A. Preparation of cell colonies

The colonies were prepared by shedding disaggregated low density (30 000–40 000 cells ml^{-1}) Vero cells (passage 165–180) in a culture medium consisting of Roswell Park Memorial Institute (RPMI 1640) medium with 10% fetal bovine serum (FBS). Both RPMI and FBS were filtered with a sterile Sartorius 0.20 μm filter to prevent the presence of inert particles that may become obstacles to the propagation of the colony front. In all cases, cell cultures were maintained at 37 °C in a 5% carbon dioxide and 95% humidity atmosphere, changing one half of the culture medium every 2 days. The latter was carefully done using a micropipette to extract 1 ml of the medium while the cells, which are adhered to the bottom of the polystyrene Petri dish (36 mm diameter), remained covered by the rest of the medium. This procedure ensured that the colony was not perturbed along the experiment.

B. Preparation of initial linear colony fronts

For the preparation of linear colony fronts, two different procedures were utilized to determine whether the cell concentration at the initial front had any influence on the colony growth dynamics. In procedure I, Vero cells were seeded on a 20×5 mm^2 thin 100-μm-thick rectangular glass plate located in a Petri dish. After reaching confluence, the glass plate was carefully transferred to a second Petri dish (procedure Ia), covered with fresh culture medium, and then the colony was left to grow from the thin glass plate edges toward the rim of the Petri dish. Alternatively, in some experiments the confluent glass was put upside down on the second Petri dish (procedure Ib), so that the colony continued growing from a front located at the bottom level of the Petri dish.

In procedure II a Teflon tape, instead of a glass plate, was employed to create the starting linear colony front (Fig. 1). Thus, the bottom of a Petri dish was centrally covered by 2.2-cm-wide and 100-μm-thick sterilized Teflon tape [Fig. 1(a)]. Then, the cells were seeded and the colony was left to grow for about 2 days until confluence on the Teflon-free region was reached [Fig. 1(b)]. Finally, the Teflon tape was removed, leaving a cell-free central region with the formation of two facing linear colony fronts of width L that started to shift in opposite directions [Fig. 1(c)]. At this stage both the changes in the colony pattern morphology and the growth front displacement were determined [Fig. 1(d)].

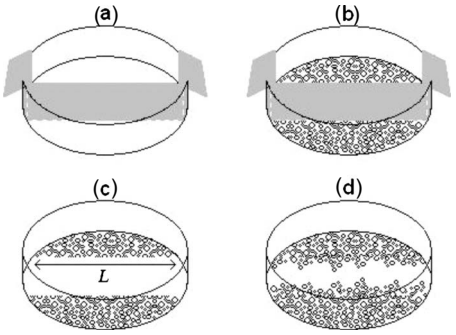

FIG. 1. Scheme of the experimental setup for procedure II: (a) Petri dish centrally covered by a Teflon tape (gray); (b) confluent cells (black dots) covering the Teflon tape-free surface of the Petri dish; (c) after withdrawing the Teflon tape, two linear growth fronts are formed; (d) two colonies growing on both sides of initially linear fronts.

It should be noted that there is always a lag time before a measurable colony growth front displacement is observed. The lag time for procedure Ia was about 48 h, presumably the sliding down average time of cells moving from the glass plate upper face to reach the Petri dish bottom. For procedures Ib and II the lag time was about 2 h. In all cases, the front displacement time scale was set to $t=0$ after the appropriate lag time correction.

C. Microscopy imaging of cell colonies

Colony growth fronts were imaged daily using a Canon digital camera coupled to a Nikon TS100 phase-contrast inverted microscope with a CFI flat field ADL 10× objective. Due to the narrow field of the objective, the entire colony image, with a resolution of 1 μm=1.13 pixel, was obtained by stitching and composing a number of partial digital images. The colony growth was followed until its propagation front contacted a small cell cluster that was generated far from the colony front from those few cells that occasionally escaped from the colony, being transported by the medium outward. This interference, which appeared after 5–8 days of growth, determined the end of the experiment.

For tracing colony front profiles, cells were considered as part of the profile when they contacted the colony through either cytoplasm or filopodia. To check for errors in tracing front profiles, digital image processing software and a Wacom graphic tablet for hand tracing were utilized. From both procedures, reproducible results with less than 1% error were obtained.

D. Experiments involving fixed and stained colonies

Colony front data from sequentially imaged colonies were checked by measuring the colonies after fixation and staining. This additional information allowed us to highlight the cytoplasm of individual cells, to improve the detection of multinuclear large cells and cell filopodia, and to evaluate the statistical distribution of both two-dimensional (2D) cell size and cell aspect ratio, the latter defined as the cell width-to-length ratio.

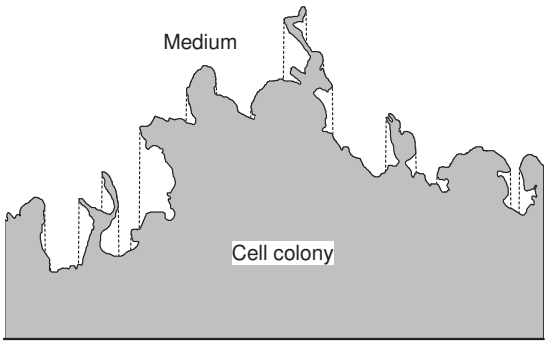

FIG. 2. Scheme of a rough 2D profile. Real (full trace) and overhang-corrected (dashed trace) profiles are indicated.

For this purpose, from an initial batch of colonies prepared according to procedure II, everyday a set of four colonies was separated, fixed, and stained with May-Grünwald Giemsa. The viability of cells, particularly the multinuclear ones, was confirmed by means of the Tripan Blue exclusion test.

Data plotted from fixed and stained colonies correspond to mean values obtained from the four colonies analyzed for each growth time. They include the standard error bars.

E. Data processing

From colony front profiles, the instantaneous colony height (h) at each site i ($i=1,2,\ldots,N$) of the starting front of width L was determined. Then, the average height $\langle h\rangle$ at time t and the average front displacement velocity ($\langle v\rangle = d\langle h\rangle/dt$) were determined. The local, $w(l,t)$, and global, $w(L,t)$, roughness and the fractal dimension D_F of each colony front were determined in the range $10 \leq l \leq L$ μm, where the value of L depended on the experimental procedure. Dynamic scaling analysis of both experimental and overhang-corrected (single-valued) colony profile data was done. Single-valued profiles were obtained from experimental data by taking the maximum value of h at each site i along L (Fig. 2). To surmount the uncertainty in the value of exponent α derived from the conventional dynamic scaling analysis of roughness fluctuations, this value was also obtained from the analysis of the structure factor of the front profile.

III. RESULTS

A. Evolution of colony patterns

Generally, the morphology of Vero cell colony patterns consists of inner irregular 3D cell domains that linearly expand as monolayer domains with a rough growth front in contact with the medium. The expansion of the monolayer domain essentially proceeds by cell duplication, at both the bulk and the front domain, assisted by changes in the size and aspect ratio of cells, as described further on. Typical changes in the cell colony growth patterns are shown in Figs. 3(a)–3(e).

For $t=2880$ min [Fig. 3(a)], the colony growth pattern displays a rather irregular and compact monolayer of small cells of approximately 26 μm average diameter and a

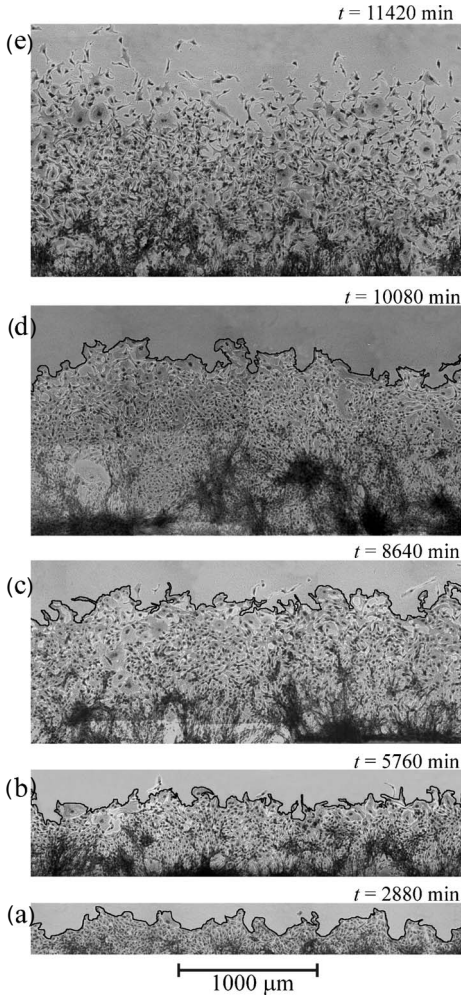

FIG. 3. Vero cell colony growth patterns at different t's obtained from fixed and stained linearly growing colonies. A fraction of the culture width L at t is shown. Black 3D cell and gray 2D monolayer domains can be seen. Cell nuclei are seen as black dots. (a)–(d) The colony front profiles are highlighted (black trace). No reliable front profile from (e) can be determined, as referred to in the text.

growth front showing protrusions and valleys. A smaller contribution of 3D domains can be observed close to the starting growth line. For $t=5760$ min [Fig. 3(b)], the expanding monolayer exhibits domains with rounded elongated cells with some cell-free areas in between, and a few large cells, most of them multinuclear, preferentially located near the growth front, contributing to local disorder. For $t>8000$ min [Figs. 3(c) and 3(d)] the density of large cells increases; some of them acquire a fibroblastlike shape, while others produce filopodia that maintain cell contact with the bulk colony. These patterns also show that the colony front expands in both the parallel and perpendicular directions to the initial front resulting in the formation of overhangs, as seen from the evolution of front profiles. The average size of the overhangs is on the order of the average cell size at t and increases with t.

Eventually, for $t=11\,420$ min [Fig. 3(e)], the protrusion and valley front morphology becomes partially distorted due to the appearance of both outlier cells and a complex net-

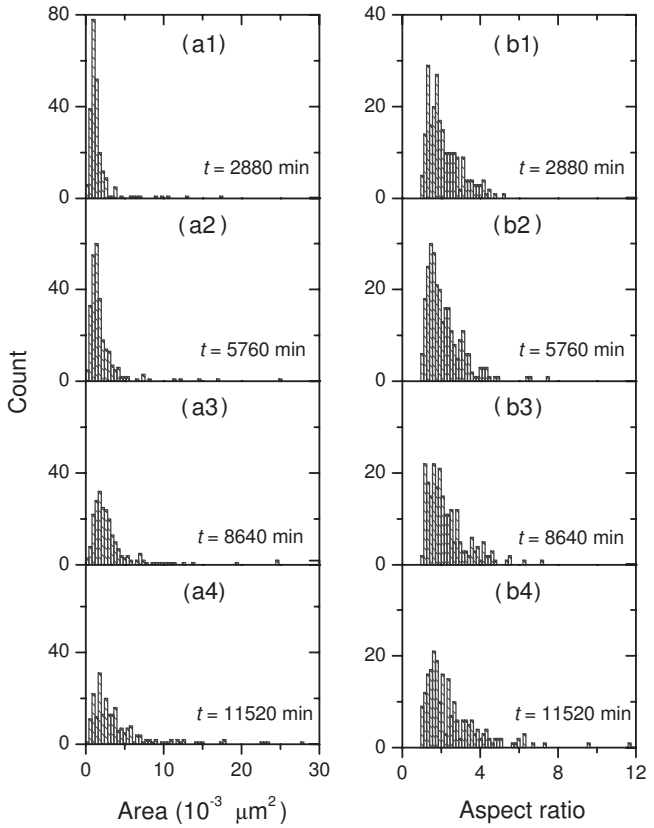

FIG. 4. Distributions of (a1)–(a4) Vero cell size and (b1)–(b4) aspect ratio at the colony front region $\langle h \rangle \pm 20\%$ in front height and $\Delta l \approx 3000$ μm in front width at different growth times.

work of interconnected cells producing voids in the neighborhood of the colony front. When this complex network sets in, the perception of the colony profile becomes uncertain. Likewise, in this case, outlier cells separated from the bulk colony form isolated clusters radially growing at a certain distance from the colony front. As the latter shifts forward, it can eventually reach those clusters and incorporate them into the colony, also determining the time at which the experiment is discontinued.

The microscopic images depicted in Fig. 3 revealed that the approximate size of the cells varied from approximately 200 μm^2 at $t < 2000$ min to about 8500 μm^2 at $t > 10\,000$ min. Furthermore, the largest cell size of about 12 000–18 000 μm^2 has also been observed for $t > 5000$ min. The above changes in cell morphology are accompanied by the appearance of spatiotemporal cell density gradients that set in the colony, seemingly assisting local flows of cells from the bulk to the colony front. It should be noted that, besides the limitations in studying the evolution of colony profiles due to the colony growth age, the size of the colony front (L) also plays a key role, as for a sufficiently low value of L, the colony tends to grow radially as most cell colonies in nature do.

B. Cell size and aspect ratio evolution

Both the cell projected area [Fig. 4(a)] and the cell aspect ratio [Fig. 4(b)] distributions, measured at the colony front region $\langle h \rangle \pm 20\%$ in front height and $\Delta l \approx 3000$ μm in front width, are consistent with changes in cell morphology (Sec. III A). At $t = 2880$, the histograms exhibit an asymmetric bell-like profile [Figs. 4(a1) and 4(b1)], with their maximum values shifting toward higher areas with t, as expected for a progressive increase in the number of large cells in the colony. Accordingly, the heterogeneity of the cell colony pattern increases with t (see Fig. 3).

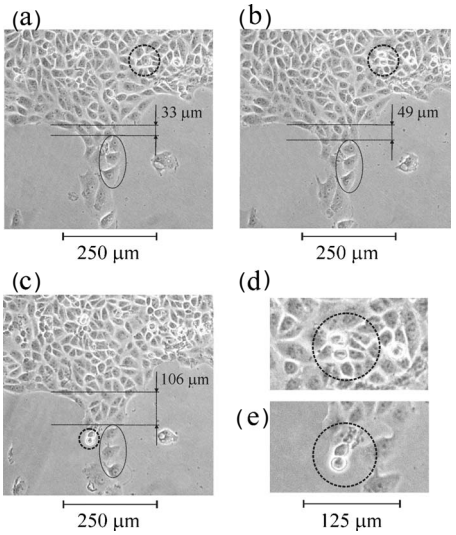

FIG. 5. Local sequential images taken at (a) $t = 151$, (b) 213, and (c) 391 min. Cell duplication (dotted circles) occurs [(a) and (b)] in the bulk and (c) at the colony front. Magnified details of cell duplications from (b) and (c) are also shown in (d) and (e), respectively. The downward shift distance of cells enclosed in the ellipses indicates that the relative shift of cells at protrusions is faster than at valleys. Relative shift distances are indicated.

C. *In situ* sequential imaging of colony patterns

Additional features of colony growth to establish where cell divisions occur and how the growth front changes locally with t were investigated utilizing cell colonies prepared from procedure II. These colonies, after 2 days of growth, were placed into a transparent closed chamber at 37 °C, under an air(95%)+CO_2(5%) flowing mixture to reproduce the incubator conditions. This chamber was properly adjusted to the microscope stage to image a selected cell monolayer domain every 10 min for 72 h. This sequential imaging demonstrates that cell division proceeds at both the bulk [Figs. 5(a) and 5(b), circled regions] and the growth front of the colony [Fig. 5(c), circled regions]. During mitosis, after shrinking, the cell mother divides into daughter cells that expand nearby without losing contact with the bulk colony through a cooperative displacement; all these phenomena result in the expansion of the front. Details of cell duplication in the bulk and at the colony front are depicted in Figs. 5(d) and 5(e), respectively.

At longer t, the local cell concentration gradients produced by distinct random duplication of cells at the inner and outer monolayer domains promote a faster shift of the growth front at protrusion sites [Figs. 5(a)–5(c)]. A scheme of local cell colony displacements is depicted in Figs.

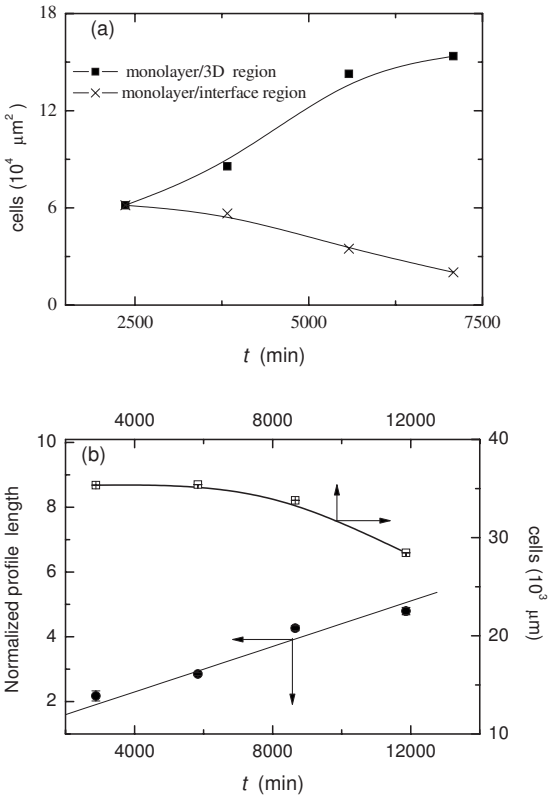

FIG. 6. (a) Cell density versus time plots for a 20×10^4 μm^2 section at the monolayer/interface and the monolayer/3D regions; (b) colony profile length normalized with respect to the colony width L, and linear cell density (number of cells/L) versus time plots for the colony front.

5(a)–5(c): the three cells enclosed in the ellipse shift faster than those at the valley front located on the left side of the image. The global colony pattern also demonstrates that cells from 3D domains contribute to increasing cell population at the monolayer, a possibility that depends on both the available space at the 2D cell domain to allocate new cells and the relative values of the cell-substrate and cell-cell interaction energies at each domain [25–28].

D. Evolution of the front profile length and cell density at the colony front and in the bulk

Colony patterns in Fig. 3 show that the cell density in the bulk increases with t and decreases toward the front of the colony. The cell density variations referred to above are consistent with the development of local density gradients, mainly in the h direction, which assists in driving local flows of cells from the monolayer bulk toward the colony front. Considering two identical rectangular monolayer domains, one from the 3D/2D boundary upward and another from the colony front downward, it follows that the cell density increases in the former region and decreases in the latter, as t increases [Fig. 6(a)].

For condensed systems it is usually admitted that an increase in surface roughness implies an increase in the number of particles at the interface. However, for a Vero cell colony the situation becomes rather different because of the change in the cell average size and shape with t. Accordingly, while the extent of the front profile relative to the width L increases almost linearly with t, the average linear density of cells at the interfacial region decreases with t [Fig. 6(b)], in qualitative agreement with the cell size and aspect ratio distribution histograms at the growth front (Fig. 4).

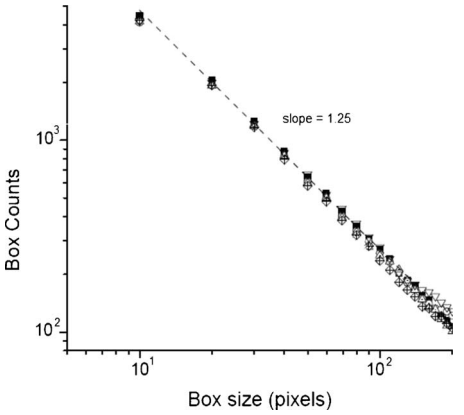

FIG. 7. Box count versus box size log-log plot for colony fronts at different growth times: (▲) 2880, (▼) 4200, (□) 5820, (■) 7320, (△) 8640, (▽) 11 820, and (⊠)12900 min.

E. Fractal dimension of colony fronts

Considering that the colony front width L is always much larger than $\langle h\rangle$, the value of D_F was determined by the box-counting method with box sizes in the range 10–200 μm (cell average size of $\simeq$26.5 μm), resulting in $D_F=1.25\pm0.05$, irrespective of both t and the experimental procedure (Fig. 7).

F. Colony front displacement velocity

Colony front average height $\langle h\rangle$ versus t plots fit reasonable straight lines with constant average front velocity $\langle v\rangle=0.22\pm0.02$ μm min^{-1}, irrespective of procedure I or II (Fig. 8). For our front width L, this figure becomes independent of the presence of overhangs and higher than 0.085 μm min^{-1}, although the latter has been reported for the radial growth of Vero C-type cell colonies in a different culture medium [8].

IV. INTERPRETATION AND DISCUSSION

A. Overview of Vero cell colony growth

The dynamic behavior of cell colony growth can be disclosed by comparing scaling exponents derived from the analysis of growth front profile data to the predictions of theoretical growth models proposed for nonbiological systems [2,4]. However, for such a procedure it is interesting to consider first some distinctions inherent to each one of those systems. Thus, condensed phase growth models usually refer to single-type pointlike depositing particles impinging on the growing phase from the outside. In contrast, the colony is made of cells, with their sizes being on the order of few tens of microns, a fact that imposes scaling cutoffs for this sys-

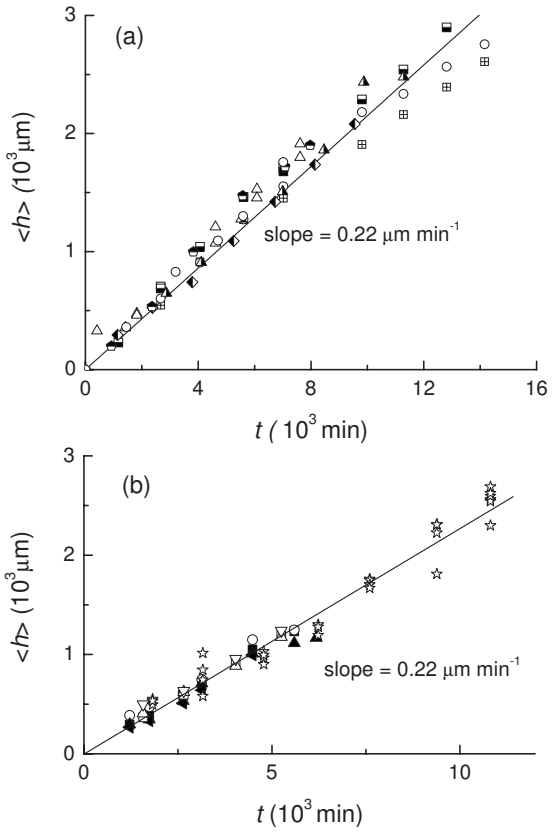

FIG. 8. Plots of $\langle h \rangle$ versus t of the colony front profiles. (a) Data from procedure I; (b) data from procedure II. Symbols correspond to different colonies for $1 \leq L \leq 2$ cm.

tem. Furthermore, depending on whether one deals with either a phase aggregation or a disruption process [2], models consider that particles can be either attached to or detached from the phase. However, the growth of a cell colony undergoes by the progressive aggregation of cells produced by cell divisions in the colony. These cells involve functional supramolecular systems that are endowed with a degree of complexity, cooperative organization, and recognition capacity [29] that exceeds those found in simpler nonbiological systems. Furthermore, the entire evolution of the cell colony involves not only the participation of interacting forces at the molecular and atomic level among different constituents, but also the contribution of mass transport processes driven by either chemical or electrochemical potential gradients [30]. Cell colony growth is also accompanied by cell disruption, which often appears as a random process involving a single or a few cells per event. These cells continue growing producing a new separated colony and fortuitously becoming again a part of the original one.

The above distinct features between biological and nonbiological systems become evident in the growth patterns of Vero cell colonies both at the 3D and monolayer cell domains. For colonies formed according to procedure Ia, the contribution of 3D domains close to the growth front at $t=0$ is enhanced with respect to procedures Ib and II, as for procedure Ia the progressive displacement of cells from the top of the glass plate to the Petri dish bottom favors the accumulation of cells there. Seemingly, this distinct feature is not reflected in the evolution characteristics of the colony studied in this work, at least within the error of the experimental data. In fact, colony growth patterns comprise intermediate stages such as the accumulation and accommodation of newborn cells. As concluded from sequential growth patterns (Fig. 5) cell duplication occurs at both the growth front level and at inner cell domains, a process that is preceded by a shrinkage of the mother cell and creation of a transient cell-free space around it. Once mitosis takes place, two daughter cells appear and adjust their shapes to become a part of the colony. As the cell population increases, changes in shapes and sizes of individual cells contribute to building up growth patterns of increasing complexity making the interactions among colony constituents more intricate. Then, local cell density gradients both in the bulk and at the colony front [Figs. 6(a) and 6(b)] induce local mechanical stresses and push the growth front forward [28]. As the colony age increases, the pushing effect is accompanied by the appearance of large cells (Fig. 4). Further complications would still arise if local advection contributions were involved [31,32]. This colony growth picture contrasts with the idea that growth front shift is governed just by cell division at the growth front, as in the case of the Eden model [33,34].

Considering the possible surface diffusion of cells, the *in situ* sequential local imaging of colony growth fronts shows that the average traveling distance of a single cell at a protrusion with respect to a reference line (Fig. 5) after 5 h is about 60 μm. Then, considering an average cell diffusion coefficient $D \simeq 10^{-12}$ cm^2 s^{-1} [21,35,36] the expected cell linear shift for $t=72$ h would be about 5 μm. Therefore, the linear cell shift velocity, which is faster than the expectation of a simple cell surface diffusion in the growth front, can be related to either cell crawling or a contribution of a local cooperative cell transport in the colony. This process should be assisted by spatially correlated noise associated with the average cell cycle, which for Vero cells is on the order of 24–48 h.

The colony fronts exhibit a fractal dimension $D_F = 1.25 \pm 0.05$ (Fig. 7), a figure that is consistent with a self-affine fractal object. However, due to the presence of overhangs, mainly caused by the size and shape of Vero cells, the front profiles are not strictly self-affine, i.e., expressible as a single-valued function [2]. Accordingly, the analysis of the colony fronts will be performed considering the experimental profiles with overhangs first and then after overhangs, correction.

Thus, from the preceding analysis it can be concluded that any interpretation and conclusion derived from a straightforward comparison of the colony front experimental data to the predictions from condensed phase growth models should cautiously be considered [2,4], particularly regarding the possible existence of cutoffs.

B. Quantitative approach to the colony roughness dynamics

In principle, the roughness dynamics of a condensed phase can be characterized by a set of scaling exponents resulting from scale invariant properties of certain physical quantities [2]. The instantaneous colony front roughness

$w(L,t)$ can be determined from the root-mean-square of the front height fluctuations

$$w(L,t) = \left\{ \frac{1}{N} \sum [h_i - \langle h \rangle]^2 \right\}^{1/2}, \quad (1)$$

with N being the number of h values comprised in the initial colony profile width L, h_i is the value of h at site i ($i=1,2,\ldots,N$), and $\langle h \rangle$ is its average value. Starting from a flat surface, the value of $w(L,t)$ for $t \ll t_s$, with t_s being the roughness saturation time, is expected to increase as

$$w(L,t) \propto t^{\beta} \quad [t \ll t_s]. \quad (2)$$

Then, for a fixed value of L, the roughness is expected to reach a saturation value. If L is changed, the saturation roughness w_s should depend on L according to

$$w_s(L) \propto L^{\alpha} \quad [t \gg t_s]. \quad (3)$$

The value of t_s depends on the system size ($t_s \sim L^z, z=\alpha/\beta$) [2].

From the scaling exponents α and β resulting from Eqs. (2) and (3), the Family-Vicsek dynamic scaling relationship [37] can be obtained for describing the growth process

$$w(L,t) \propto L^{\alpha} f\left(\frac{t}{L^z}\right). \quad (4)$$

Equation (4) should bring about the collapse of roughness data.

A coherent set of exponents serves as indication of the likely universality class of the process [2]. It should be noted that Eq. (4) involves all modes including the contribution of the noncritical short-wavelength modes. This means that in Eq. (4) one would expect a strong finite-size dependence [38], and therefore it is always convenient to complement the analysis with the determination of the structure factor of the front profile, as described further on.

The preceding analysis, however, implies the existence of a single-valued rough profile. Neither overhangs nor time-dependent changes in size and shape of active particles are considered. As discussed above, these facts constrain a straightforward quantitative interpretation of the scaling exponent data from our experiments.

1. Roughness front profile plots from experimental data

A tentative dynamic scaling analysis of experimental data following Eq. (2) results in w versus t log-log plots yielding reasonable straight lines. From the least-squares linear regression of the experimental points in the range 200–15 000 min a slope $\beta=0.33$ is obtained with a standard error of 0.02, irrespective of the experimental procedure [Fig. 9(a)]. Otherwise, these plots show no clear roughness saturation. On the other hand, the w versus l log-log plots [Fig. 9(b)] result in sigmoid curves that show an inflection point at $l=l_{c/c}$, which is localized in the range 30–60 μm, i.e., close to the average cell size at time t. No value of exponent α can be obtained from these plots. Correspondingly, from the latter, one can conclude that the growth kinetics of cell colonies produced by either procedure I or II appears to be the same, although the initial roughness of colonies resulting from the former becomes higher than that from the latter.

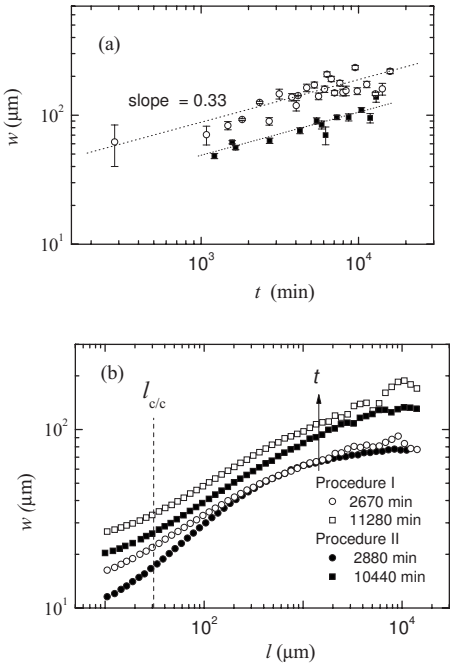

FIG. 9. Scaling plots from experimental (without overhang correction) data. (a) log w versus log t. (b) log w versus log l. Colonies grown according to procedures I (white symbols) and II (black symbols). The dashed line at $l_{c/c} \simeq 30$ μm determines a lower cutoff that divides the plot into two regions: the single cell domain ($l < l_{c/c}$) and the colony domain ($l > l_{c/c}$). The arrow indicates increasing values of t. For the sake of clarity data have been binned.

2. Dynamic scaling exponents from overhang-corrected data

The w versus l log-log plots [Figs. 10(a) and 10(b)] resulting from overhang-corrected data show an initial linear increase from $l=10$ to approximately 30 μm, which scales with exponent $\alpha' = 0.85 \pm 0.05$, irrespective of both t and the experimental procedure. This scaling exponent, related to $l < l_{c/c}$, can be associated with the membrane of a single cell, which is expected to be under roughness saturation at the time range of the experiments. The study of this domain is beyond the scope of this work.

The w versus l log-log plots for the net colony domain, which appears for $l > l_{c/c}$, exhibit a smooth curvature downward with the trend to a limiting w value that increases with t. This trend, which is better observed at lower values of l and t, confirms that the growth of the colony domain undergoes under no saturation conditions. However, for values of l in the range $150 \leq l \leq 1100$ μm and $t > 8000$ min (Fig. 10), the w versus l log-log plots tend to approach a slope close to 0.5 as t increases, irrespective of the experimental procedure. To confirm whether this figure can be related to a true local roughness exponent, it was evaluated from the structure factor, as described further on.

The existence of the above cell and colony domains becomes also evident from the w versus t log-log plots of overhang-corrected data at different l's (Fig. 11). In this case,

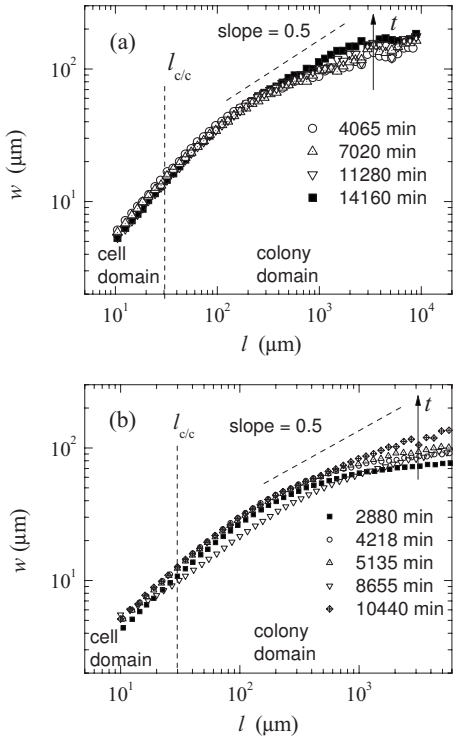

FIG. 10. log w versus log l plots for overhang-corrected data from (a) procedure I and (b) procedure II. The arrows indicate the shift of the curves as time increases. The straight lines with a slope of 0.5 are drawn to guide the eye. Data have been binned for the sake of clarity.

reasonable straight lines in the range 10 μm$\leq l \leq L$, with slopes increasing from nearly zero for $l=10$ μm up to $\beta = 0.33 \pm 0.02$ for $l > 500$ μm, are obtained. The latter coincides, within the experimental error, with the value of β resulting from roughness data without overhang correction for $l=L$ [Fig. 9(a)]. The dependence of β on l indicates that a reliable value of β is obtained when l largely exceeds the width of the cell membrane domain, i.e., in agreement with the distinct culture domains indicated in Fig. 10.

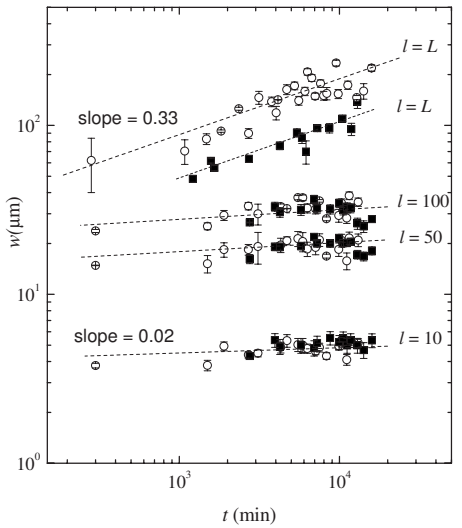

FIG. 11. log w versus log t plots from overhang-corrected data from procedure I (white symbols) and procedure II (black symbols). L values correspond to the colony width. Values of l are given in μm. Data have been binned for the sake of clarity.

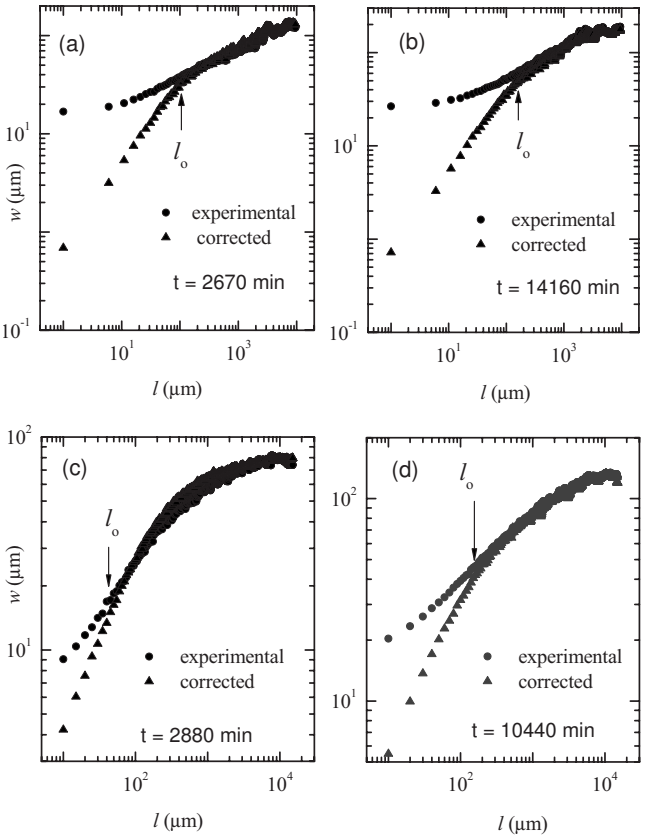

FIG. 12. Comparison of w versus l log-log plots from experimental and overhang-corrected data from [(a) and (b)] procedure I and [(c) and (d)] procedure II. Values of l_0 at each t are indicated. Within the error of the experiments, for $l > l_0$, experimental and overhang-corrected data overlap.

3. Comparison of dynamic scaling plots from experimental and overhang-corrected data

The comparison of w versus l log-log plots (Fig. 12), resulting from experimental and overhang-corrected data, shows the overlapping of both plots when l exceeds a critical value l_o, which increases with t and determines the width of the colony beyond which the growth dynamics becomes practically insensitive to overhangs. The reverse effect occurs for $l < l_o$. Therefore, the influence of overhangs over the entire colony front smears out as l increases, with the colony roughness approaching the behavior of a single-valued profile. The shift of l_o with t can then be assigned to the increase in the density of overhangs as the roughness increases with t.

4. Power spectra of colony profiles

The scaling behavior of the colony profile can also be evaluated from the structure factor $S(k,t)$ of the single-valued profiles [39,40]

$$S(k,t) = \langle \hat{h}(k,t)\hat{h}(-k,t) \rangle, \tag{5}$$

where

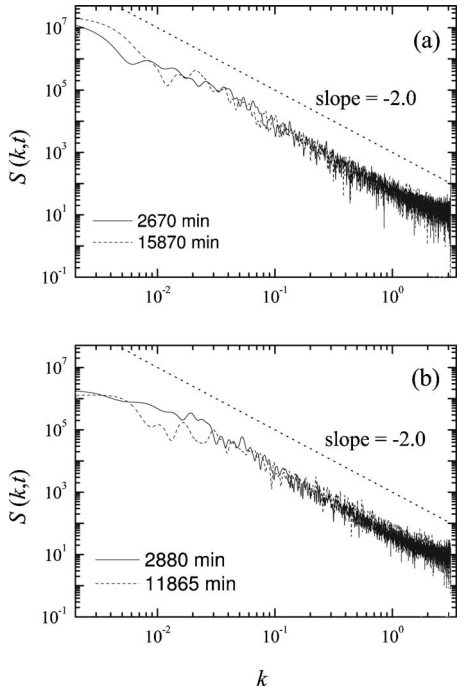

FIG. 13. log $S(k,t)$ versus log k plots for colony fronts resulting from (a) procedure I and (b) procedure II. For the sake of clarity only spectra corresponding to colony fronts near the initial and final stages of growth are depicted. The straight lines with a slope of $-(2\alpha+1)=-2$ are drawn to guide the eye.

$$\hat{h}(k,t) = \frac{1}{\sqrt{L}} \sum_{x} [h(x,t) - \langle h \rangle] e^{ikx} \tag{6}$$

is the kth Fourier mode of the profile height around its average value at t.

Furthermore, in the Fourier space, in the absence of any critical length scale, the Family-Vicsek relationship can be expressed in terms of $S(k,t)$ [22,39,41],

$$S(k,t) = k^{-(2\alpha_s+1)} f(tk^{1/z}), \tag{7}$$

where α_s is the global roughness exponent and, for $x=tk^{1/z}$,

$$f(x) = \begin{cases} \text{const} & \text{for } x \gg 1 \\ x^{-(2\alpha+1)} & \text{for } x \ll 1. \end{cases} \tag{8}$$

The $S(k,t)$ versus k log-log plots from different overhang-corrected colony front data (Fig. 13) are rather noisy as has been often observed [8], but their distribution in the range $0.02 \leq k \leq 1$ approaches a common straight line with a slope close to -2, which corresponds to $\alpha_s = 0.50 \pm 0.05$, irrespective of both t and the experimental procedure. Unfortunately, no further conclusions about any displacements of spectra neither with t nor with l can be drawn from these plots, as one would expect for an anomalous scaling effect [39].

C. Likely growth dynamics of Vero cell colonies

Experimental data from colony patterns reveal new variables, such as the cell size and shape spatiotemporal distributions in the colony, and the existence of a cutoff determining the relevance of the cell and the colony domains that are involved in the dynamics of the growth process. This sort of complexity is beyond the theoretical framework of simplified classical growth models and at present becomes a drawback to have a coherent picture of the colony growth kinetics, despite the fruitful efforts that have been made on the subject seeking fuller integration of systems biology [14,42,43].

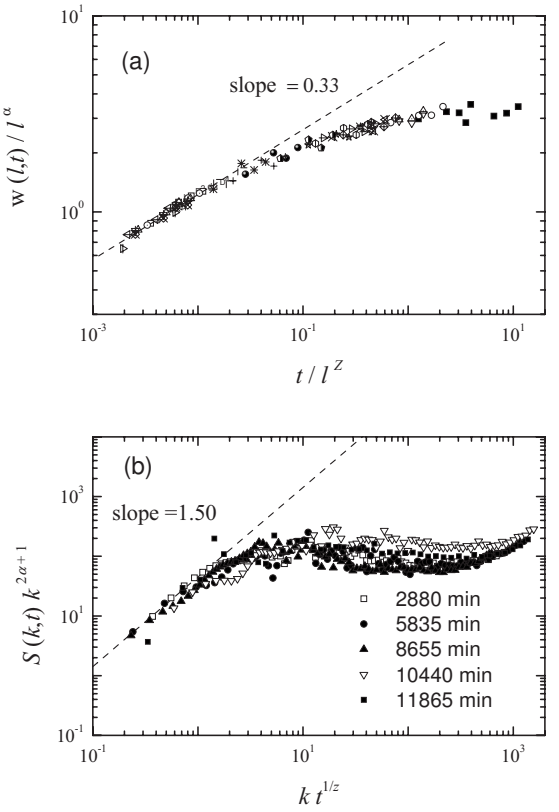

FIG. 14. Log-log plots of Family-Vicsek scaling relationships [Eqs. (4) and (7)] for $\alpha=0.5$ and $z=1.5$. The values of t indicated in (b) are representative of the different stages of the colony growth. Data have been binned for the sake of clarity.

The analysis of Vero cell colony linear growth fronts, resulting from the spatiotemporal dependence of experimental (Fig. 9) and overhang-corrected (Figs. 11 and 13) data reported in this work, allowed us to evaluate reproducible scaling exponents $\beta \simeq 0.33 \pm 0.02$ and $\alpha_s \simeq 0.50 \pm 0.05$ for $l > 200$ μm. This set of exponents makes it possible to infer a likely mechanism accounting for the colony growth dynamics. Within the experimental errors, this set of exponents fulfills the Family-Vicsek relationships (Fig. 14) and is consistent with the values of those exponents are close to those predicted by nonlinear surface growth continuous models comprised in the Kardar, Parisi, and Zhang (KPZ) universality class, i.e., $\beta=0.33$ and $\alpha=0.50$ [44]. This is also consistent with the fact that, although the w versus l log-log plots exhibit no clear scaling, the curves slowly tend to the slope of 0.5 as t increases (Fig. 10). This behavior is qualitatively comparable to that found from the numerical simulation of ballistic deposition (KPZ universality class) [45].

The KPZ equation for the growth of a rough colony front under linear velocity comprises three contributions:

$$v(h,t) = \frac{\partial h(x,t)}{\partial t} = \nu \nabla^2 h + \frac{\lambda}{2}(\nabla h)^2 + \eta(x,t). \quad (9)$$

The first *right-hand side* term represents the surface relaxation (smoothing term), involving a surface tension coefficient ν, which contributes to reducing irregularities at the rough profile changing the average protrusion height. In this case the smoothing process may also involve surface diffusion of cells (conservative process). This overall surface relaxation effect involves the change in the cell site coordination number (cn) in going from protrusions (lower cn) to valleys (higher cn). The influence of cn appears both in the cell division and in the daughter cell accumulation and allocation processes, as well as in the kinetics of cell surface diffusion. These effects, particularly in the colony front, should depend on the radius of curvature of front irregularities [2].

The second nonlinear term contributes to increasing the lateral growth area of protrusions (nonconservative process). In this case, the addition of material ($\lambda > 0$), from either cell duplication or cell size increase, or cell displacements in the colony bulk at lateral parts of protrusions, where the local slope is larger, increases the average height of the colony front. The third term is the Gaussian noise $\eta(x,t)$ at the growth front. Discarding Brownian motion as a significant contribution to the shift of the colony growth front, $\eta(x,t)$ should mainly be related to the stochastic division of cells. This process is characterized by the average cell cycle time, which depends on a number of other cell features that are beyond the scope of this work. Therefore, when the cell size and shape distribution changes along the colony growth, Eq. (9) becomes extremely complicated. For example, in this case, a collection of cell cycle times should be expected, at variance with a homogeneous average-size cell colony.

Finally, the validity of the KPZ dynamics for the growth of Vero cell monolayer colonies, although limited for $l > 200$ μm, is—in principle—coherent with the cellular automata model recently advanced [22], in which cell division and pushing, and migration effects on an irregular lattice are taken into account [21,22]. This model assumes that cell division is not restricted to the front of the colony and that migration of cells is triggered by the division of one of them in order to minimize mechanical stress in the neighborhood. These features are, to some extent, also consistent with the results reported in our work.

V. CONCLUSIONS

Some experimental strategies are proposed to investigate the linear growth of cell monolayer colony fronts and are applied to study the dynamics of Vero cell colonies. The results show that the growth patterns of a Vero cell colony consist of both 3D and cell monolayer domains, and the cell division occurs in both the bulk and at the colony front. The distributions of both cell size and shape change with the colony age. As time increases, large and elongated cells appear, particularly at the colony front. Furthermore, *in situ* sequential local growth patterns show distinct cell division stages, cell displacements and reaccommodations in the colony, and local outward flows of cells. The shift of the colony front is assisted by the local flow of cells driven by cell concentration and pressure gradients in the bulk. The growth fronts exhibit overhangs of the size of the average cell diameter upward and a fractal dimension $D_F = 1.25 \pm 0.05$.

The log w versus log l plots resulting from experimental data show a sigmoid curve with an inflection point at a value of $l_{c/c}$ close to the average diameter of a cell. This value determines a lower domain of the front where the roughness properties are dominated by cell membrane fluctuations. At $l \gg l_{c/c}$, those properties are related to the colony front fluctuations. The comparison of w versus l log-log plots from experimental and overhang-corrected data shows a characteristic length l_o that determines the front width where the influence of overhangs is negligible. The value of l_o can be related to the average size of protrusions and valleys. Scaling exponents $\alpha = 0.5 \pm 0.05$ and $\beta = 0.33 \pm 0.02$ are derived from conventional dynamic scaling and Fourier analyses. These exponents, within the experimental error, fulfill the Family-Vicsek relationship and are close to those predicted by the KPZ model for $l > 200$ μm. It should be noted that although not all the issues involved in the colony growth are explicitly included in the KPZ equation, it formally appears that it is adequate to capture the essentials of the dynamic behavior of this complex system.

ACKNOWLEDGMENTS

The authors thank Dr. S. Coronato for her assistance in Vero cell culture preparation and Dr. C. Horowitz for comments and manuscript reading. This work was financially supported by the Consejo Nacional de Investigaciones Científicas y Técnicas (CONICET) (Grant No. PIP 2231), Agencia Nacional de Promoción Científica y Técnica (ANPCYT) (Grant No. PICT 34530), and the Comisión de Investigaciones Científicas de la Provincia de Buenos Aires (CICPBA).

[1] D. Farin and D. Avnir, in *The Fractal Approach to the Heterogeneous Chemistry*, edited by D. Avnir (Wiley, Chichester, 1989), p. 271.

[2] A. L. Barabasi and H. E. Stanley, *Fractal Concepts in Surface Growth* (Cambridge University Press, Cambridge, England, 1995).

[3] N. G. V. Kampen, *Stochastic Processes in Physics and Chemistry* (Elsevier, Amsterdam, 1992).

[4] P. Meakin, *Fractals, Scaling and Growth Far From Equilibrium* (Cambridge University Press, London, 1998).

[5] R. V. Solé and S. C. Manrubia, *Orden y Caos en Sistemas Complejos* (Ediciones Universitat Politécnica de Catalunya,

Barcelona, 1996).
[6] J. Schmittbuhl, J.-P. Vilotte, and S. Roux, Phys. Rev. E **51**, 131 (1995).
[7] A. Brú, J. M. Pastor, I. Fernaud, I. Brú, S. Melle, and C. Berenguer, Phys. Rev. Lett. **81**, 4008 (1998).
[8] A. Brú, S. Albertos, J. L. Subiza, J. L. García-Asenjo, and I. Brú, Biophys. J. **85**, 2948 (2003).
[9] P. Meakin, J. Theor. Biol. **118**, 101 (1986).
[10] F. Fujikawa and M. Matsushita, J. Phys. Soc. Jpn. **58**, 3875 (1989).
[11] M. Matsushita and H. Fujikawa, Physica A **168**, 498 (1990).
[12] M. Matsushita, J. Wakita, H. Itoh, I. Ráfols, T. Matsuyama, H. Sakaguchi, and M. Mimura, Physica A **249**, 517 (1998).
[13] T. Vicsek, M. Cserzo, and V. K. Horvath, Physica A **167**, 315 (1990).
[14] M. Radszuweit, M. Block, J. G. Hengstler, E. Schöll, and D. Drasdo, Phys. Rev. E **79**, 051907 (2009).
[15] A. Brú and D. Casero, J. Theor. Biol. **243**, 171 (2006).
[16] E. Izquierdo-Kulich and J. M. Nieto-Villar, Math. Biosci. Eng. **4**, 687 (2007).
[17] B. Brutovsky, D. Horvath, and V. Lisy, Physica A **387**, 839 (2008).
[18] J. Buceta and J. Galeano, Biophys. J. **88**, 3734 (2005).
[19] A. Brú, Biophys. J. **88**, 3737 (2005).
[20] J. M. Pastor and J. Galeano, Cent. Eur. J. Phys. **5**, 539 (2007).
[21] D. Drasdo and S. Höhme, Phys. Biol. **2**, 133 (2005).
[22] M. Block, E. Schöll, and D. Drasdo, Phys. Rev. Lett. **99**, 248101 (2007).
[23] R. Sheets, FDA Technical Report, 2000 (unpublished).
[24] A. T. Nahapetian, J. M. Thomas, and W. G. Thilly, J. Cell. Sci. **81**, 65 (1986).
[25] E. Paluch, J. van der Gucht, and C. Sykes, J. Cell Biol. **175**, 687 (2006).
[26] M. Aubert, M. Badoual, S. Féreol, C. Christov, and B. Grammaticos, Phys. Biol. **3**, 93 (2006).
[27] Y.-S. Chu, O. Eder, W. A. Thomas, Y. Sincha, F. Pincet, A. Ben-Ze'ev, E. Perez, J. P. Thiery, and S. Dafour, J. Biol. Chem. **281**, 2901 (2006).
[28] T. Rosen and D. S. Misfeldt, Proc. Natl. Acad. Sci. U.S.A. **77**, 4760 (1980).
[29] M. Ahlers, W. Müller, A. Reichert, H. Ringsdorf, and J. Venzmer, Angew. Chem., Int. Ed. Engl. **29**, 1269 (1990).
[30] *Physical Chemistry of Biological Interfaces*, edited by A. Baszkin and W. Norde (Marcel Dekker, Inc, New York, 2000).
[31] M. A. Pasquale, J. L. Vicente, S. L. Marchiano, and A. J. Arvia, J. Phys. Chem. B **108**, 13315 (2004).
[32] D. Dan, C. Mueller, K. Chen, and J. A. Glazier, Phys. Rev. E **72**, 041909 (2005).
[33] M. Eden, *Proceedings fo teh 4th Berkeley Symposium on Mathematical Statistics and Probability*, edited by F. Neyman (University of California Press, Berkeley, CA, 1961), p 223.
[34] J. Kertesz and D. E. Wolf, J. Phys. A **21**, 747 (1988).
[35] J. C. M. Mombach and J. A. Glazier, Phys. Rev. Lett. **76**, 3032 (1996).
[36] D. Beysens, G. Forgacs, and J. A. Glazier, Proc. Natl. Acad. Sci. U.S.A. **97**, 9467 (2000).
[37] F. Family and T. Vicsek, J. Phys. A **18**, L75 (1985).
[38] D. Liu and M. Plischke, Phys. Rev. B **38**, 4781 (1988).
[39] J. J. Ramasco, J. M. López, and M. A. Rodríguez, Phys. Rev. Lett. **84**, 2199 (2000).
[40] J. M. López, M. A. Rodríguez, and R. Cuerno, Physica A **246**, 329 (1997).
[41] J. M. López, M. A. Rodríguez, and R. Cuerno, Phys. Rev. E **56**, 3993 (1997).
[42] C. Escudero, Phys. Rev. Lett. **102**, 139602 (2009).
[43] O. Wolkenhauer, C. Auffray, S. Baltrusch, N. Blüthgen, H. Byrne, M. Cascante, A. Ciliberto, T. Dale, D. Drasdo, J. D. Fell, J. E. Ferrell, D. Gallahan, R. Gatenby, U. Günther, B. D. Harms, H. Herzel, C. Junghanss, M. Kunz, I. van Leeuwen, P. Lenormand, F. Levi, M. Linnebacher, J. Lowengrub, P. K. Maini, A. Malik, K. Rateitschak, O. Sansom, R. Schäfer, K. Schürrle, C. Sers, S. Schnell, D. Shibata, J. Tyson, J. Vera, M. White, B. Zhivotovsky, and R. Jaster, Cancer Res. **70**, 12 (2010).
[44] M. Kardar, G. Parisi, and Y.-C. Zhang, Phys. Rev. Lett. **56**, 889 (1986).
[45] C. Horowitz (private communication).